University of the Basque Country

Master's in Nanoscience

www.mscnano.eu

MASTER THESIS

Terahertz time domain spectroscopy of diabolo antennas

by

Katarína Rovenská

Supervisor: Dr. Rainer Hillenbrand

Date of defense: 10$^{\text{th}}$ July 2019

PREFACE

This thesis was developed within my stay at CIC nanoGUNE, San Sebastian, which was supported by the Erasmus+ project. The aim of my work at CIC nanoGUNE was to contribute to the PETER project (Plasmon Enhanced Terahertz Electron paramagnetic Resonance), funded by the *Future and Emerging Technologies (FET Open)* section of the *Horizon 2020*, which is the biggest of the *EU Research and Innovation* programmes, supporting the early-staged scientific research of ideas towards new technologies. The main goal of the PETER project is to combine plasmonic field enhancement at THz frequencies with electron paramagnetic resonance (EPR), in order to introduce a novel method for the characterization of the paramagnetic substances. To that end, the highly enhanced magnetic component of the electromagnetic field provided by plasmonic diabolo antennas will enable to conduct EPR measurements with enhanced sensitivity and unprecedented spatial resolution [1].

The presented thesis deals with the initial steps of the PETER project and describes the main outcomes of the work I have done within five months of my six-month stay at CIC nanoGUNE. This was mainly focused on the plasmonic part of the project, specifically on the fabrication of micro-scale plasmonic diabolo antennas via direct laser writing and the characterization of these antennas by the means of terahertz time domain spectroscopy (THz-TDS).

ACKNOWLEDGEMENTS

My work in CIC nanoGUNE has been supervised by Dr. Rainer Hillenbrand, whom I would like to express my gratitude in the first place: many thanks for your patience, provided corrections and guidance, especially in the early weeks of my stay, when nothing worked the way it should. Dr. Monika Goikotxea, a great thank you for making sure my stay at nanoGUNE was as seamless as possible. Dr. Shu Chen, thank you for the consultations regarding the antenna designs, the insight of a theoretician was very helpful. Also I would like to thank the people who provided me with trainings necessary for my work, Ralph Gay and Dr. Christopher Tollan. To nanooptics group members: thank you for making a great work environment, I enjoyed the time spent with you. Lastly, I would like to thank my family and friends: Ďakujem, že ste mi pripomínali domov a podporovali ma.

CONTENTS

1 INTRODUCTION

Based on interaction processes between electromagnetic (EM) radiation and conduction electrons at metallic interfaces, a new branch in the field of nanophotonics has been formed, called plasmonics [2,3]. Among others, plasmonics is mainly interested in two types of quasiparticles: surface plasmon polaritons (SPP) and localized surface plasmon polaritons (LSPP).

SPP is an interaction of the surface plasmon (collective oscillation of the charge density at metal-dielectric interface) with a photon [4]. Experimentally, effects corresponding to SPPs have been observed since the beginning of 20th century, first as unexpected decrease in intensity of light reflected from metallic gratings by Wood [5]. Explanation of this concern was given by Ritchie et al. in 1968, stating that the existence of collective oscillations of conduction electrons is the responsible element [6].

LSPPs represent the interactions of collective electron oscillations with photons, localized and bounded to a metallic structure. Historically, the first appearance of the effects caused by LSPPs are dated back to the Roman era. The glass in the Lycurgus cup contains silver and gold colloidal nanoparticles which causes this cup to appear in two different colors, distinguishable when observed in the transmitted or the reflected light [7]. More commonly, the use of the nanoparticles can be seen in church windows, as metallic nanoparticles have been used for staining of glass troughout past eras. The concept of LSPPs has been in theory demonstrated by Mie in 1908 [8]. The fundamental principles of the field of plasmonics, devoted mostly to the description of these two quasiparticles, are discussed in chapter 2.

Nowadays, plasmonic structures find application in various fields: optoelectronics [9], data storage [10], photovoltaics [11], ... and spectroscopy, namely the use in Surface-Enhanced Infrared Absorption Spectroscopy SEIRA [12,13] and Surface-Enhanced Raman Scattering SERS [14,15] as means for biosensing is progressive. The key-attribute of a plasmonic structure is the enhancement of the EM field in its surroundings [16] and the confinement of EM radiation below sub-wavelength dimensions [17]. However, both mentioned properties are conditioned by the resonance of the LSPP occuring in the structure. To yield a plasmonic structure with a specific resonance wavelength, all its physical attributes need to be thought trough, as the dimensions and materials used within the structure and its substrate define the spectral position of the resonance in the EM spectrum. The shape of the antenna also affects the resonance, inspiring further research of nanorods [13,15,18], nanotriangles [19,20], nanodiscs [12,21] or three-dimensional nanostructures [14,22].

Majority of the previously mentioned experiments refers to the visible and infrared region of the EM spectrum. The reasons for that are natural, visible light and its properties are investigated by mankind since the ancient times, as it is the only

part of EM spectrum percievable by the naked eye. Current research in this topic is concerned with stealth technologies [23], fabrication of biomimetric structures [24] or anticounterfeiting features [25]. On the other hand, infrared region allows non-destructive targetting of unique vibrational fingerprints of numerous molecules [26]. Most of the research is therefore devoted to developing various nanostructured surfaces enabling the enhanced sensing of molecules [27, 28], and even portable devices serving those purposes [29, 30]. Infrared frequencies also find applications in waveguides or in photovoltaic cells [31–33].

Recently, the field of research in the terahertz (THz = 10^{12} Hz) region expands, as this region of EM spectrum offers nondestructive and nonionizing radiation suitable for medical and biological applications [34, 35]. Many materials have their fingerprint-like spectra in this spectral region, which makes the THz frequencies suitable for sensing and detection purposes [36–38]. The emerging characterization method of paramagnetic substances within the THz frequency region is researched within the PETER project, as mentioned in the Preface. The presented thesis aims to contribute to this project and therefore, topics related to the project framework form the core of this thesis.

Chapters 3 and 4 are devoted to the description of the done experimental work. First, chapter 3 provides detailed technical information about the tool used for THz time domain spectroscopy (THz-TDS). As this instrument has been designed for different purposes, a thorough analysis of the tool is provided to facilitate the work of others willing to use this setup for THz-TDS. Datasets yielded from the measurement require processing in order to provide information about the plasmonic resonances of the measured structures. The used processing methods are discussed at the end of chapter 3. Within the chapter 4, the fabrication process of the antennas is described, along with the optimalization steps, which were taken in order to achieve diabolo antennas of high quality, with resonances within the $(0.2 - 1.4)$ THz region. The results of the antenna fabrication are presented, accompanied by an analysis of the preparation method accuracy.

The final chapter is focused on the results and presents the influence of several attributes of the fabricated antennas on the plasmonic resonances measured by THz-TDS. First, the impact of the substrate and antenna separation on the resonance peak position and magnitude is shown, followed by the study of diabolo antenna size influence on the resonant wavelength. A linear dependence has been derived from the experimental results, which can serve for accurate fabrication of diabolo antennas with specified resonance wavelength. Lastly, a summary of all the done work is provided in Conclusions.

2 BASICS OF PLASMONICS

Once a metallic structure is exposed to electromagnetic radiation of a specific frequency, the electromagnetic field in its close proximity is enhanced. In this chapter, the fundamental theoretic background corresponding to this phenomena will be explained.

2.1 Optical properties of metals

By the term optical properties of materials, usually the responses of materials towards the electromagnetic field are meant. These are expressed in a form of the complex dielectric function:

$$\varepsilon(\omega) = \varepsilon'(\omega) + i\varepsilon''(\omega), \tag{1}$$

where $\varepsilon'(\omega)$ and $\varepsilon''(\omega)$ correspond to its real and imaginary part, respectively, dependent on ω, the frequency of the EM wave. Commonly, plasmonic structures are fabricated out of semiconductors with high free charge carrier concentration or metals, the latter being the case of this thesis. Hence, the dielectric function used for description of metals is introduced in the following.

2.1.1 Dielectric function of the Drude-metal

The Drude model of a metal, often reffered to as a plasma model, is based on the assumption of free electron gas moving against the fixed positive ion core background. The electrons are affected by an external electric field $\mathbf{E}$, which forces them to oscillate. However, their motion is damped – the model accounts for the electron collisions occuring in the material with a collision frequency $\gamma = 1/\tau$. The mean relaxation time τ of the electrons in metal is usually $\sim 10^{-14}$ at room temperature. According to the second Newton law, the motion equation of a Drude-electron is:

$$m\ddot{\mathbf{x}} + m\gamma\dot{\mathbf{x}} = -e\mathbf{E}, \tag{2}$$

where m represents the electron mass, $\ddot{\mathbf{x}}$ and $\dot{\mathbf{x}}$ represent the acceleration and the velocity of the electron, respectively, and $-e$ corresponds to the charge of an electron. Solving this equation with the assumption of harmonic external electric field $\mathbf{E}$ leads to:

$$\mathbf{x}(t) = \frac{e}{m(\omega^2 + i\gamma\omega)}\mathbf{E}(t). \tag{3}$$

This can be used to derive the polarization $\mathbf{P}$, occuring as the electrons (electron concentration denoted as n_e) move against the positive ion cores:

$$\mathbf{P} = -ne\mathbf{x} = -\frac{n_e e^2}{m(\omega^2 + i\gamma\omega)}\mathbf{E}. \tag{4}$$

Taking into account the material relationships among the electric field induction $\mathbf{D}$, the electric field intensity and polarization: $\mathbf{D} = \varepsilon_0\mathbf{E} + \mathbf{P}$ and $\mathbf{D} = \varepsilon_0\varepsilon\mathbf{E}$, the dielectric function of metals according to Drude model can be expressed as:

$$\varepsilon(\omega) = 1 - \frac{\omega_p^2}{\omega^2 + \mathrm{i}\gamma\omega},\tag{5}$$

where $\omega_p = (n_e e^2/\varepsilon_0 m)^{1/2}$ is the plasma frequency of the free electron gas.

2.2 Surface plasmon polariton

A surface plasmon polariton (SPP) is a longitudinal oscillation of the charge at the interface of a metal and a dielectric, caused by a collective reaction of the electrons to an external factor, such as an electromagnetic wave or a different electron. To introduce this problem, a simple geometry will be used: a linear interface between dielectric and metal semiinfinite spaces, as suggested in Fig. 1. The derivation of the conditions, which need to be fulfilled in order to enable the existence of a SPP is thoroughly described in [2,3,7]. Therefore, this work will present only the main outcomes regarding the surface plasmon polariton theory.
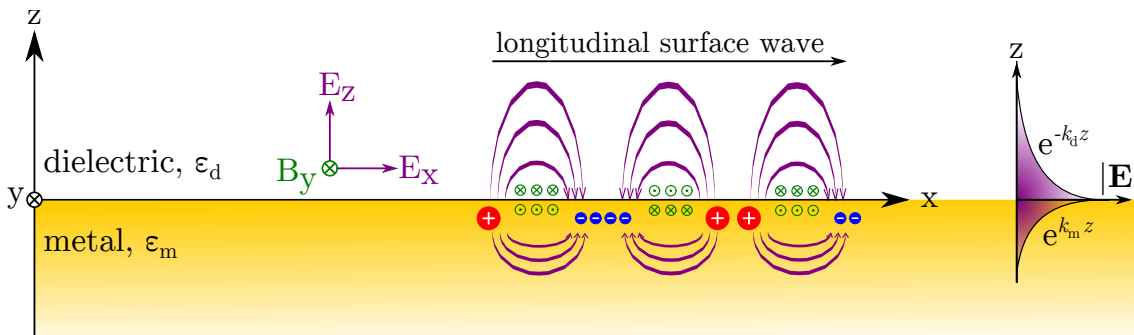

Fig. 1: Surface plasmon polariton on the interface between a dielectric and a metal.

The fact that SPP are bounded to the dielectric-metal interface is in conflict with the TE (transverse electric or s-) polarization of the SPP. Hence, only the TM (transverse magnetic or p-) polarization of the SPP can exist, with three nonzero field components: H_y, E_x and E_z (shown in Fig. 1 and described in the Table 2.1). The TM polarization is governed by the TM wave equation:

$$\frac{\partial^2 H_y}{\partial^2 z} + \left(k_0^2\varepsilon - \beta^2\right) H_y = 0,\tag{6}$$

where $k_0 = \omega/c$ is the wave vector of the EM wave propagating in vacuum and β is the propagation constant of the SPP, basically the x-component of the SPP wave vector, c representing the speed of light in vacuum.

Field components in the dielectric ($z > 0$)	Field components in the metal ($z < 0$)
$H_y(z) = \mathrm{e}^{\mathrm{i}\beta x}\mathrm{e}^{-k_\mathrm{d}z}$	$H_y(z) = \mathrm{e}^{\mathrm{i}\beta x}\mathrm{e}^{k_\mathrm{m}z}$
$E_x(z) = \mathrm{i}\dfrac{k_\mathrm{d}}{\omega\varepsilon_0\varepsilon_\mathrm{d}}\mathrm{e}^{\mathrm{i}\beta x}\mathrm{e}^{-k_\mathrm{d}z}$	$E_x(z) = -\mathrm{i}\dfrac{k_\mathrm{m}}{\omega\varepsilon_0\varepsilon_\mathrm{m}}\mathrm{e}^{\mathrm{i}\beta x}\mathrm{e}^{k_\mathrm{m}z}$
$E_z(z) = -\dfrac{\beta}{\omega\varepsilon_0\varepsilon_\mathrm{d}}\mathrm{e}^{\mathrm{i}\beta x}\mathrm{e}^{-k_\mathrm{d}z}$	$E_x(z) = -\dfrac{k_\mathrm{m}}{\omega\varepsilon_0\varepsilon_\mathrm{m}}\mathrm{e}^{\mathrm{i}\beta x}\mathrm{e}^{k_\mathrm{m}z}$

Tab. 2.1: Nonzero components of the EM field in the TM polarisation, k_d and k_m denote those components of the SPP wave vector in the dielectric and the metal, respectively, which are perpendicular to the interface of the two media. The exponential damping of the electric field along the z-direction is shown in Fig. 1 with purple graph.

As the continuity of the field components at the interface must be preserved, three conditions for the SPP wave vector components arise when the respective magetic field components are inserted into (6):

$$\frac{k_d}{k_m} = -\frac{\varepsilon_d}{\varepsilon_m}, \tag{7a}$$

$$k_d^2 = \beta^2 - k_0^2\varepsilon_d, \tag{7b}$$

$$k_m^2 = \beta^2 - k_0^2\varepsilon_m. \tag{7c}$$

Equations stated in (7), when combined, lead to the dispersion relation of a SPP:

$$\beta = k_0\sqrt{\frac{\varepsilon_d \cdot \varepsilon_m}{\varepsilon_d + \varepsilon_m}}. \tag{8}$$

Considering real propagation vector β and real wavevector k_0, the equation (8) demands the $\varepsilon_m < -\varepsilon_d$. Hence, SPP occurs only at the interface of materials with opposite signed dielectric function, such as a metal and a dielectric. Inserting the model of dielectric function of a metal with neglected damping factor (eq. (5) with $\gamma = 0$) into (8) introduces a limit SPP frequency:

$$\omega_{SPP} = \frac{\omega}{\sqrt{1 + \varepsilon_d}}. \tag{9}$$

Based on the equation (8), another important outcome can be derived. The SPP propagation factor can be expressed as:

$$\beta = \frac{2\pi}{\lambda}n_\mathrm{eff}, \tag{10}$$

where λ represents the wavelength of the initial EM wave and

$$n_\mathrm{eff} = \sqrt{\frac{\varepsilon_d \cdot \varepsilon_m}{\varepsilon_d + \varepsilon_m}} \tag{11}$$

is the effective refractive index. As it includes both the dielectric functions of the dielectric and the metal acting at the interface, it may be considered one of the characteristics of optical properties arising at the dielectric-metal interface.

2.3 Localised surface plasmon polariton

Fig. 1 depicts the propagation of a SPP along the infinite metal-dielectric interface. However, when SPP occurs in finite-sized metallic structure, the propagation of the wave is limited by the structure boundaries. As the SPP is localised in the plasmonic structure, the name *localised surface plasmon polariton* (LSPP) is commonly used for description of this phenomenon. However, the term LSPP resonance should be reserved only for the resonances occuring in sub-wavelength-sized particles at the Fröhlich frequency, $\omega_F = \omega_p(1 + 2\varepsilon_d)^{-1/2}$ [3] and the term Fabry-Perot resonances should be used instead. As the opinions on this subject vary across the scientific community, the expression LSPP will be used to describe the spatially restricted SPP within this thesis on behalf of the author.

In special cases, when the wavelength of the initial EM wave $\lambda = jL$, with j being a positive integer, a "stationary wave" is formed at the surface, resulting into a resonance of the LSPP. However, the wavelength which supports the LSPP resonance in a plasmonic structure is also affected by the materials forming the structure and its dielectric environment, as introduced with SPP. This can be described by the effective refractive index identified in (11). To summarize, different resonance modes of the LSPP can be distinguished, given by the resonance wavelength:

$$\lambda_{\text{res},j} = \frac{2Ln_{\text{eff}}}{j}. \tag{12}$$

The resonance of the LSPP gives rise to the enhancement of the EM field in the metallic structure and its close surroundings. Based on the similarity with radio-antennas, plasmonic structures are often reffered to as plasmonic antennas. Antennas at non-resonant wavelengths support the enhancement of the EM field only partially – the smaller is the difference between the actual and the resonance wavelength of a structure, the greater is the EM field enhancement. This originates in the destructive interference of the induced fields, dwelling in the ability of the surface wave to propagate and oscillate at the antenna-dielectric interface. The enhancement of the electric and magnetic field by a rod-shaped plasmonic antenna supporting the LSPP resonance at $j = 1$ is depicted in Fig. 2A) by purple and green lines, respecively.

This work deals with fabrication and characterization of diabolo-shaped antennas. The diabolo shape has been chosen as it gradually compresses the width of a rod-shaped antenna, eventually creating a bridge in the middle. The spatial confinement results in high current density within the created bridge, compare the grey lines in panels A) and B) of Fig. 2. As described by the Ampère circuital law, the current density affects the induced magnetic field. Hence, the increase of the current density in the antenna's bridge area supports great enhancement of the magnetic field around
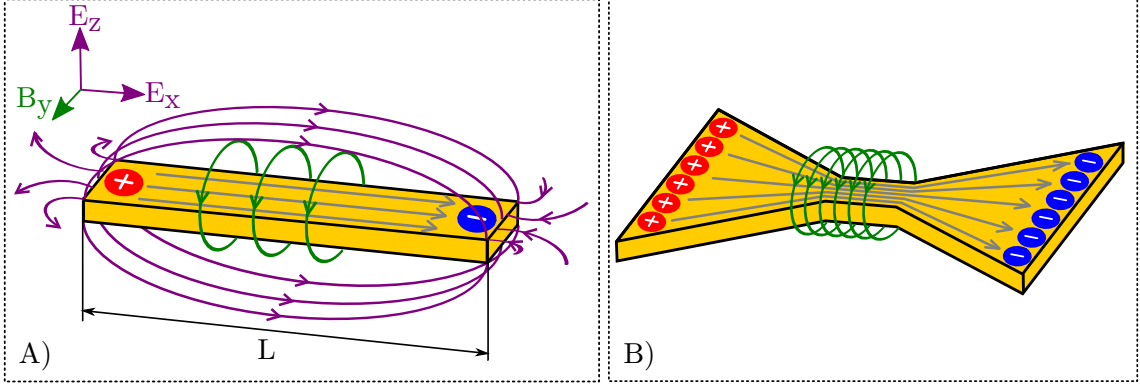
Fig. 2: Localised surface plasmon polariton – resonances. A) Rod-shaped dipole antenna. B) Diabolo shaped dipole antenna. The electric field lines are marked with purple (left out in panel B) for clarity), magnetic field lines with green. Grey lines indicate the electric current within the antennas.

it. A simulation of the field enhancement by a diabolo antenna resonant around 150 µm is shown in Fig. 3. Panel A) shows the relative electric field enhancement, most significant at the ends of the antenna wings. This is understandable, as the LSPPs have zero velocity at the ends of the antenna, as they need to turn to opposite direction in order to propagate along the antenna-dielectric interface. On the other hand, panel B) in the Fig. 3 shows the enhancement of the magnetic field. As stated afore, this is the result of the high current density in the antenna bridge. The great enhancement of the magnetic fields is one of the reasons for using the diabolo antennas within the PETER project.
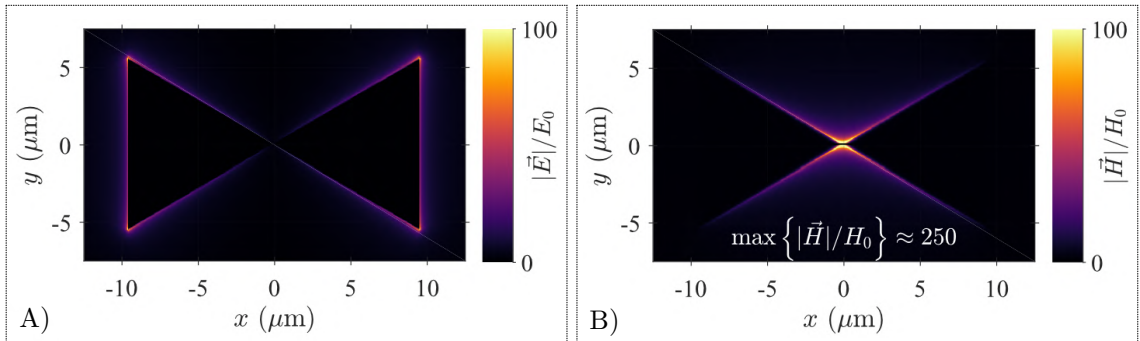

Fig. 3: FDTD simulations of a diabolo antenna supporting a LSPP resonance. A) Electric and B) magnetic field distributed around the resonant diabolo antenna. Adapted from [39].

3 THz SPECTROSCOPY

The terahertz (THz, Tera $= 10^{12}$) region of EM spectrum supports the radiation-matter interactions of wide variety in the fields of physics, biology and chemistry [36]. Its position in the EM spectrum covers the frequencies between infrared and microwave radiation, hence the range of these frequencies is commonly referred to as the THz gap, see Fig. 4. The characteristic energy of THz radiation ranges in units to tens of meV, corresponding to the events with durations of picoseconds. This enables the utilization of the THz frequencies in examination of biological samples for medical causes [35], quality control of groceries [34], detection of potentially dangerous substances such as illicit drugs or explosives [40,41] and allows the development in researching excitons, bonds of molecular crystals [42] or free charge plasma [43].
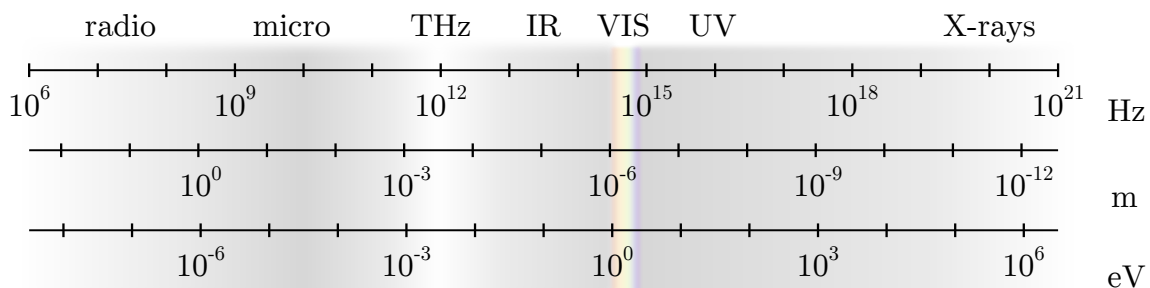
Fig. 4: A diagram of the electromagnetic spectrum.

Spectroscopy is a technique of various substances characterization, which studies the absorption/emission of EM radiation by the sample as a function of the wavelength λ of the applied radiation. A spectroscopic measurement can be performed in two different ways, using the space- or time-domain separations of the incoming signals.

The terahertz time domain spectroscopy (THz-TDS) has been used within this thesis in the THz frequency range. Fig. 5A) shows an experimental setup for THz-TDS in a reflection geometry. A femtosecond (femto $= 10^{15}$) laser pulse is sent towards the beam splitter, which divides it in two equal beams, the generating beam and the detecting beam. The generating beam serves for the optical excitation of photoconductive dipole antennas, which act as a THz radiation emitter. The THz beam is sent onto a sample and the reflected radiation follows towards the detector. The detection of the THz field is done by photoconductive sampling in an antenna within the detector, meaning that the detector needs to be "activated" by the pulse coming within the detection beam in order to record the amplitude and phase of the sample-reflected radiation. By the detection of the THz field for differently time-delayed points (realized by the change of optical path within the delay stage), an

interferogram is formed.

A typical example of the data acquired with time domain spectroscopy (TDS) is depicted in Fig. 5B)-D), which shows the THz-TDS measurement of lactose monohydrate, substance resonant at 0.3 and 0.5 THz. Fig. 5B) shows an interferogram measured with the THz-TDS setup. Using the Fourier transform, this information is converted to a spectral dependence of the measured radiation intensity, see Fig. 5C). To evaluate the data, a normalization of the gain results often takes place and the results of the experiment are then presented as normalized reflectivity (see Fig. 5D)) or normalized transmittance, based on the used spectroscopic setup.
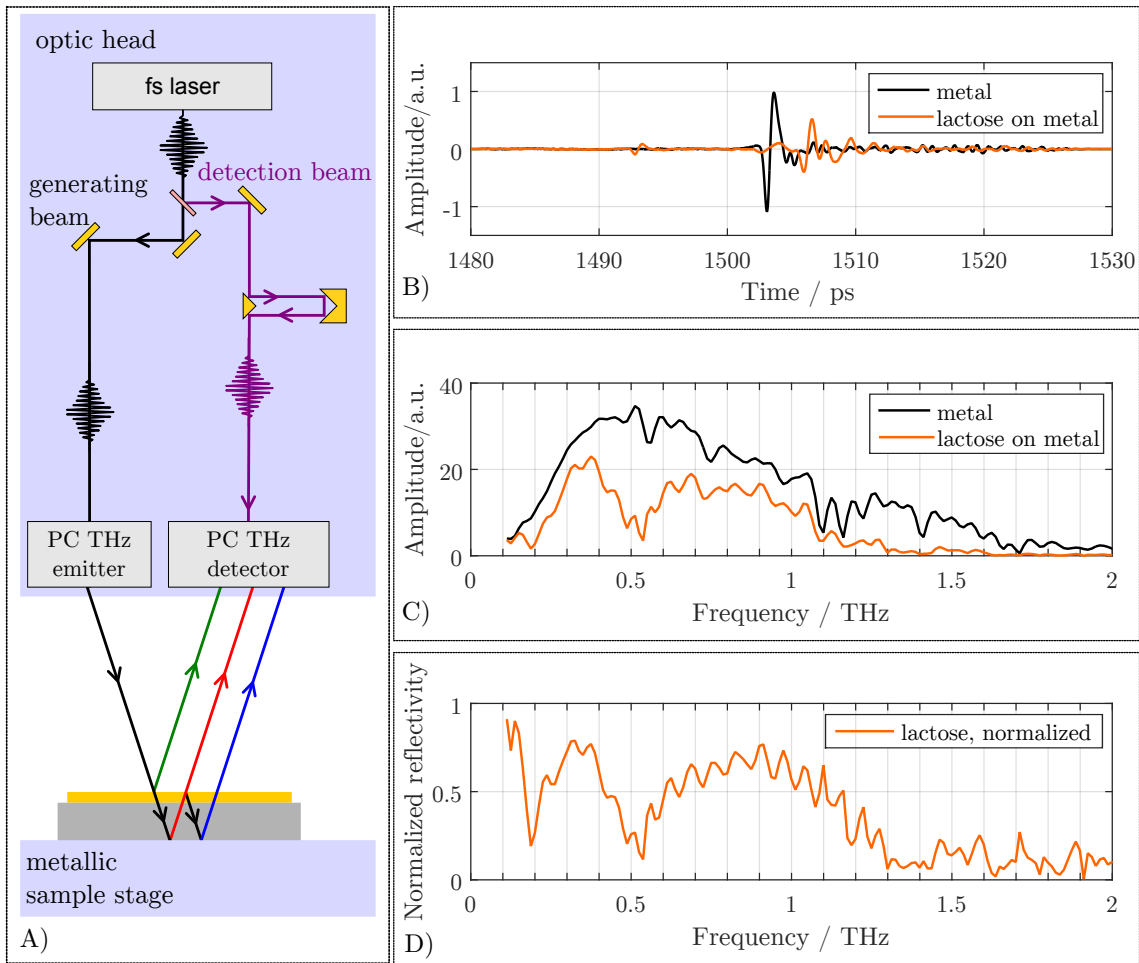

Fig. 5: Terahertz time-domain spectroscopy. A) THz-TDS setup in reflection geometry. The THz field is recorded as a function of the delay between the two beams in the system, see B) for the measurement of lactose monohydrate. C)Fourier transform of the interferograms obtained in B). D) Lactose spectrum normalized to the metal reference - resonant behavior around 0.3 and 0.5 THz can be observed.

3.1 Measurement tool

The THz-TDS measurements presented in this work have have been carried out in a reflection geometry, given by the construction of the used instrument, which has been developed by the Das Nano company, named Onyx – see Fig. 6. Although anteriorly designed for conductivity measurements of thin layers of graphene and other 2D materials, Onyx can serve to the causes of THz-TDS, as it provides interferograms coresponding to every selected point of the sample along with subsequent Fourier transform of the yielded interferograms.
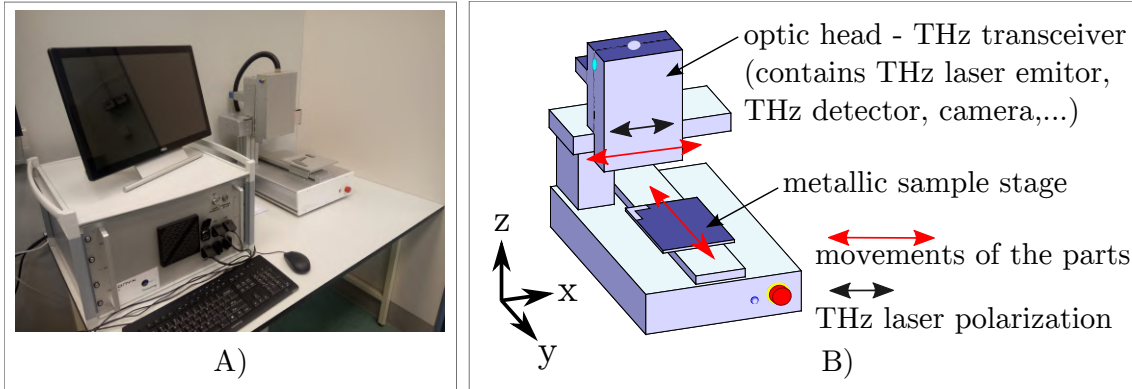

Fig. 6: Onyx instrument. A) Power supply unit (left) and the 3D positioning system (right). B) Illustrative scheme of the 3D positioning system of the Onyx instrument.

The operation of this instrument is an easy task and requires little to no training. The Onyx software allows the user to adjust solely seven settings before the measurement itself, making the system easy to operate at one side and very inflexible at the other. The adjustable settings are:

- name of the sample,
- size of the sample ($< 4''$ or $> 4''$),
- selection of the area to be measured,
- step size of the measurement,
- choice of the substrate,
- working directory for data saving,
- aquisition of the internal reference spectrum.

The following text will briefly summarize the effects of individual settings.

3.1.1 Sample name

Any text written in this field is automatically labelled with the information about the date and time of the saving (not the time of the measurement itself), i. e.: `Example_yymmdd_hhmmss`. This name is then displayed in the name of the saved

folder and the names of all the files contained in it, preventing the user from over-writing the saved data.

3.1.2 Sample size

The Onyx software allows for choosing whether the sample size is less or more than 4 inches. Based on the choice of the sample size (less or more than $4'' = 10.16$ cm), the sample photo is composed out of one ($< 4''$) or multiple parts ($> 4''$). Although the sample stage dimensions are (180×180) mm, the measured samples might be even larger, one must only care for the safety during the measurement (see the movement of the parts labelled with red in Fig. 6B)) and the software restriction about the measured area itself, see subsection 3.1.3.

The thickness of the sample, or rather the vertical distance between the measured objects and the optic head, is an important factor as well. The restriction of this parameter does not come only from the vertical space between the optic head and sample stage (ca. 35 mm during the measurement), it is much more limited by the instrument's software. The Onyx software is designed to record solely the time region of $(1480 - 1520)$ ps for the interferograms, as this interval corresponds to the time delay of the THz beam reflected from the sample stage. Hence, if the sample is too high above the sample stage surface, the disturbance in the THz pulse containing the sample response may not appear in the measured time region (i.e. the elevation of the sample by 1.2 cm is too much).

3.1.3 Measured area

The measured area must fit within the interval of values $(0 - 177.2)$ mm in the x-direction and $(0 - 180.2)$ mm in the y-direction. The null point in these intervals corresponds to the center of the screw in the upper left corner of the sample stage, which serves for anchoring the sample holder. Aside from dismantling the tool, there is no way to perform the TDS measurement without the sample stage under the sample. A beam-path changing geometries of the measurement, where sample was allocated from the metallic stage were probed, yielding unsuccesful results. The computing part of the software takes the presence of the metallic stage under the sample as granted, resulting into indistinguishable patterns on the resulting conductivity map and spectra

3.1.4 Measurement step size

The step size of the measurement may be set to: 1000 µm, 500 µm, 250 µm, 100 µm or 50 µm. A comparison of these settings is shown in Fig. 7 with notes about the time

duration of the measurement; the scanned area is (10x10) mm² large silicon sample with various gold patterns. The yielded maps suffer from two infirmities. First, the numbers at the axes ticks correspond to the number of the pixel, not a distance in mm as stated. Second, there is a displaying issue – the software automatically saves the conductivity map with pre-given space around it, resulting into incomplete displaying of the Y-axis title if there is a number with more than two digits in the Y-axis ticks, as can be seen in some of the panels in Fig. 7.

An actual resolution of this instrument is unidentified. Even though the step size can be set to 50 µm, the beam spot size is certified to be 2.1 mm on the sample stage holder, see the Appendix A - scanned Certification of calibration for the Onyx Das Nano instrument. Conductivity maps shown in Fig. 7 also point out that even with the finest step size setting, some featurs of the sample can no longer be detected, as their signal is too low to be identified from substrate in the beam spot area of 3.46 mm².
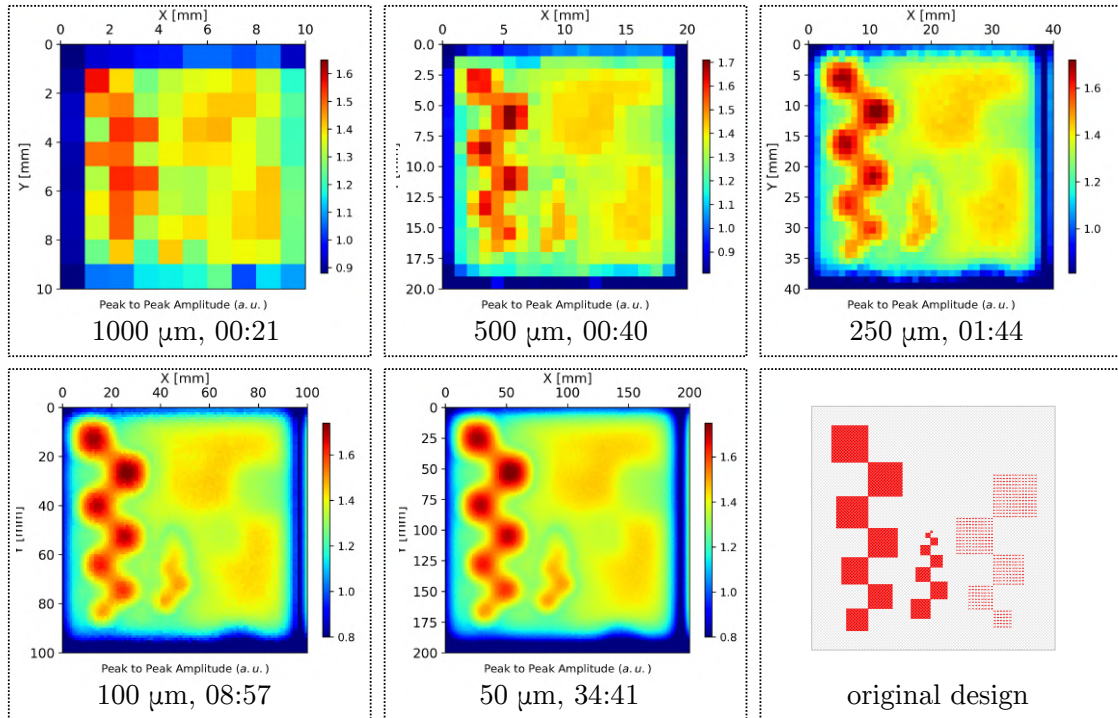

Fig. 7: Comparison of conductivity maps captured with various step size settings. Respective settings and time duration (in minutes and seconds) of each measurement are included in the corresponding panels. Sample used in this comparison was highly resistive silicon substrate with gold patterns shown in the left bottom corner of the figure. The design consists of full squares (side range: $(1500 - 100)$ µm) and arrays of diabolo antenna (antenna length $L = 65$ µm) with array side range of $(1700 - 700)$ µm.

3.1.5 Substrate choice

This setting is useful to the users willing to do the conductivity measurements. After selection of the substrate, the software produces a conductivity map while taking into account that the measured thin layer lies on a certain substrate. Aside from several pre-defined substrate types in the software, there is a possibility to create a new substrate by stating the real and imaginary part of the substrate's refractive index. At the moment, this function is disabled with no possibility of being activated. For the purposes of this work, no substrate was selected, as the samples were measured in various conditions. Measured interferograms were instead processed externally (see section 3.4).

3.1.6 Working directory

Selection of the working directory serves as a path for saving the experimental results. A folder containing files specified in Tab. 3.1 is then created at the selected location.

file content description	file extension		
measurement conditions	.csv	yes	yes
sample photograph	.png	no	yes
conductivity map	.png, .txt	yes, yes	yes, yes
interferograms of measured pixels	.h5	no	yes
conductivity map histogram	.png	yes	yes
amplitude profile of the selected line	.png	if selected	if selected
interferogram preview of selected points	.png, .csv	no	if selected
spectrum preview of selected points	.png, .csv	no	if selected

Tab. 3.1: Comparison of the data saving regimes in Onyx software.

3.1.7 Reference spectrum

Onyx software offers an opportunity to use internal reference spectrum - a special part of the sample stage in the upper right corner is dedicated to it. This setting seems to be rather a choice of safety-checking of the system than actual adjustment of the measurement. The instrument's manual states it should be run automatically before the first measurement and appear in the form of preview. This does not happen and the reference spectrum option may be therefore used solely to record the reference spectrum for analytic purposes.

3.2 Spectral range

By the term spectral range, a region of frequencies measurable by an instument is meant. This range is an intersection of the spectral ranges of all of the components in the optical path of the instrument. In some cases, several components of the instrument might be replaced by the users to alter the frequency range of the instrument and to suffice the specific needs of their experiments. As the Onyx instrument was not designed to perform measurements with the character of THz-TDS, its spectral range is strictly given by its current state. As no information regarding the components located inside the instrument is provided to the user, an experiment was conducted to establish the spectral range of the Onyx tool. Arrays of gold diabolo antennas on the quartz substrate, designed to be resonant at various THz frequencies, were measured with the Onyx setup. The results of these measurements can be seen in the Fig. 8, this experiment is discussed further in the section 5.2. Based on it, the spectral range of the Onyx instrument is estimated to be $(0.3 - 1.4)$ THz. Antennas resonant below 0.3 THz and above 1.4 THz have not been tested, but the available results advise that the spectral range might be even broader, adding approx. 0.1 THz to each of the range limits.
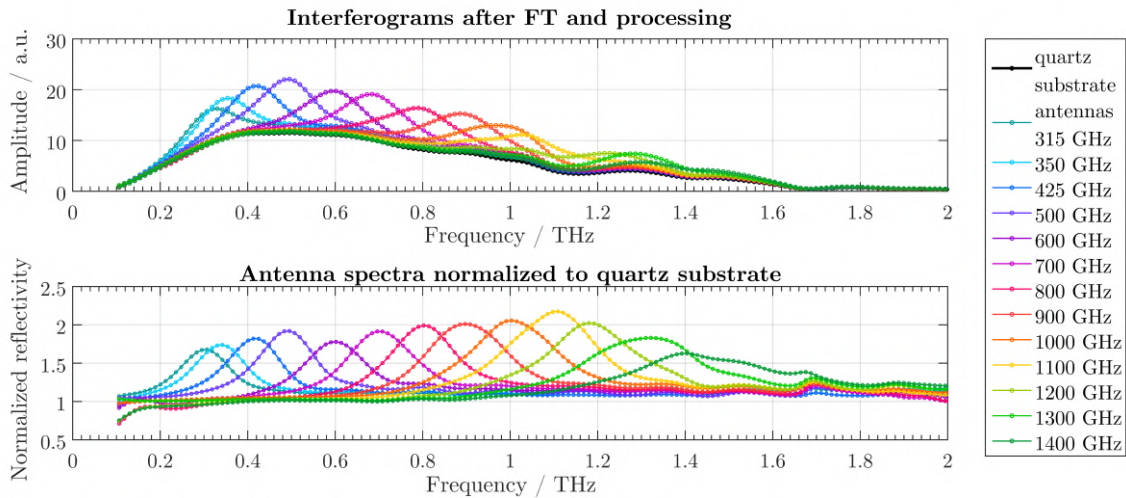

Fig. 8: Spectral range of Onyx. Based on the results of condicted experiment, the spectral range of Onyx has been estimated to $(0.3 - 1.4)$ THz. Legend shows the approximate resonance peak position.

3.3 Spectral resolution

Spectral resolution of an instrument denotes its ability to resolve features in the measured spectra. In the case of TDS, the spectral resolution is mostly given by the

length of the recorded time domain region. The spectral resolution Δf of the TDS tool can be established by analogy to the equation:

$$\Delta\omega_{\mathrm{min}}[\mathrm{cm}^{-1}] = \frac{1}{d_{\mathrm{t}}[\mathrm{cm}]}, \tag{13}$$

with $\Delta\omega_{min}$ being the spectral resolution of a standard FT spectroscopy tool and d_t the total optical path difference of the measured interferogram [44]. This equation, when adjusted to the time domain approach and converted to the units convenient to the used setup, results into simple formula:

$$\Delta f[\mathrm{GHz}] = \frac{1000}{\Delta t[\mathrm{ps}]}, \tag{14}$$

where Δf stands for the spectral resolution of a TDS instrument and Δt represents the length of the measured time domain interval. According to this, the spectral resolution of the measurement carried out with the Onyx system gives $\Delta f = 20$ GHz, as the length of recorded time domain interval is 50 ps. Although, when the data is processed, only a part of the time domain region is selected for further analysis (the one coresponding solely to the reflection at air-antenna interface, i.e. green lines in Fig. 9). The restriction of the the time domain interval has a negative influence on the yielded spectral resolution and the value of spectral resolution increases with respect to (14).

A way for decreasing spectral distance of two plotted points can be introduced by the addition of zero valued data to the end of the selected time domain region, thus artificially elongating the selected time domain interval Δt. With respect to (14), the spectral distance of two plotted datapoints has been lowered down to ca. 18% of its previous value, as the limitations were set by the size of the measured conductivity map and available computing memory. All the results presented within this thesis have been processed in a way which results into the spectral resolution $\Delta f \doteq 10$ GHz.

3.4   Processing of the collected data

For the processing of data collected during the THz-TDS measurement, an analytical software tool MATLAB has been used. Without additional data processing, the measured interferograms provide only a little to no information about the plasmonic responses of the antennas – which is the goal of the THz-TDS measurement in this case and therefore should be accomplished.

Hence, a script has been developed which applies Fourier transform on interferograms collected from every point of the measurement. To provide the results in high quality and isolate the plasmonic antenna responses from the other collected data,

several processing steps are included, described in the following subsections. First, a time domain region used for FT is specified, as using the whole measured interval for FT yields no observable antenna resonances. Before the FT itself, the selected time domain data are multiplied by an apodization function, which prioritizes the temporally earlier effects and deminishes the values of recorded ringing at the end of the selected time domain region, which originates in the instrument or the antenna sustrate. The described actions enhance the quality of the spectra in a significant way, see Fig. 9. For selected points of the conductivity map, the average spectra are created by using the spectra of the correspondive neighboring points to ensure the results reflect the actual plasmonic responses of the antennas in an accurate way. The Fourier transformed spectra are then plotted "as are" and also in their normalized nature, with respect to a selected point of reference.

Not all the mentioned data processing steps have been implemented into the MATLAB script by the author of this thesis. To clarify the origin of individual operations, the subsection 3.4.1 is devoted to the description of the script developed by Dr. Curdin Maissen, former post-doc in the CIC nanoGUNE nanooptics group, which served as a starting point for further adjustments developed by the author, described in the subsections 3.4.2 – 3.4.4.

3.4.1 The original script

The original script loads all the data included in .h5 file generated by the Onyx software and applies Fourier transform to two selected points, corresponding to the pixels of the obtained conductivity map. Fourier transform is a powerful tool which enables the decomposition of the measured temporal or spatial dependence to the corresponding frequency contributions,

$$F(\alpha) = \int_{-\infty}^{\infty} e^{i\alpha x} f(x) dx. \tag{15}$$

However, as the measurement time is finite, the developed script uses discrete Fourier transform:

$$F_k = \sum_{n=1}^{N} x_n e^{i2\pi(k-1)\frac{n-1}{N}}, \tag{16}$$

ergo the set of measured values $\{x_n\} := x_1, x_2, ...x_N$ dependent on time is transformed into a set of values dependent on frequency $\{F_k\} := F_1, F_2, ...F_N$. Within the script, the former temporal x-axis is recomputed to the frequency axis and the corresponding y-values are altered by the means of Fourier transform as already described. An option of zero-padding was introduced, enabling better resolving ability in the gained spectra by artificial addition of the zero-valued points to the end of the sequence $\{x_n\}$, this enhancement is discussed in [44]. After the Fourier transform,

the spectrum of point of interest would be divided by the reference spectrum in order to obtain normalized reflectivity of the sample point.

As described, the script was given to the author of this thesis, who made a few adjustments in order to actually observe resonances of fabricated antennas with the THz TDS setup.

3.4.2   Time domain subinterval selection

The selection of the time domain interval used for Fourier transform showed up to be crucially important. In the early starts of this work, no specific antenna resonance could be observed due to strong Fabry-Perot resonances occuring in the system. Firstly, multiple measuring strategies have been probed which would not affect the spectral resolution of the method, but as none of them led to satisfying results, the restriction within the time-domain region was put to use.

An illustrative example is shown in Fig. 9. Gold antennas on quartz substrate were measured in reflection setup, shown in Fig. 5A), and a plain quartz substrate was used for the normalization of gain results. In Fig. 9A), the results of the described measurement are shown with no addititonal processing. No resonance can be observed as a result of using the whole interferogram for the Fourier transform. However, the stated reason has been justified only after the division of the measured time domain region into individual parts coresponding to the reflections shown in Fig. 5C). When these subintervals were used for three individual Fourier transforms, shown in Fig. 9B), some clarity has been brought to the results obtained in classical data processing shown in panel A). The first and the second reflection (marked by green and red, respectively) cancel each other out and therefore, no specific resonance has been observed in the nanoantenna array. For all data processing contained in this work, the time domain region corresponding solely to the first reflection, ergo reflection at the air-antenna interface, has been taken into account for Fourier transform and further analysis.

3.4.3   Apodization

Even though the spectra shown in the Fig. 9C) already enable the observation of the plasmonic antenna responses, a lot of noise features which affect the shape of the resonance peak is still present. To eliminate these, an apodization function has been introduced: by multiplying the interferogram with this function, the parts of interferogram causing the remnant noise are devalued. Within the developed script, a half-gaussian window is implemented and its borders correspond to the borders of the selected time domain interval. The shape of the curve (the strength of the devaluation) can be controlled by adjusting a single parameter a, which corresponds
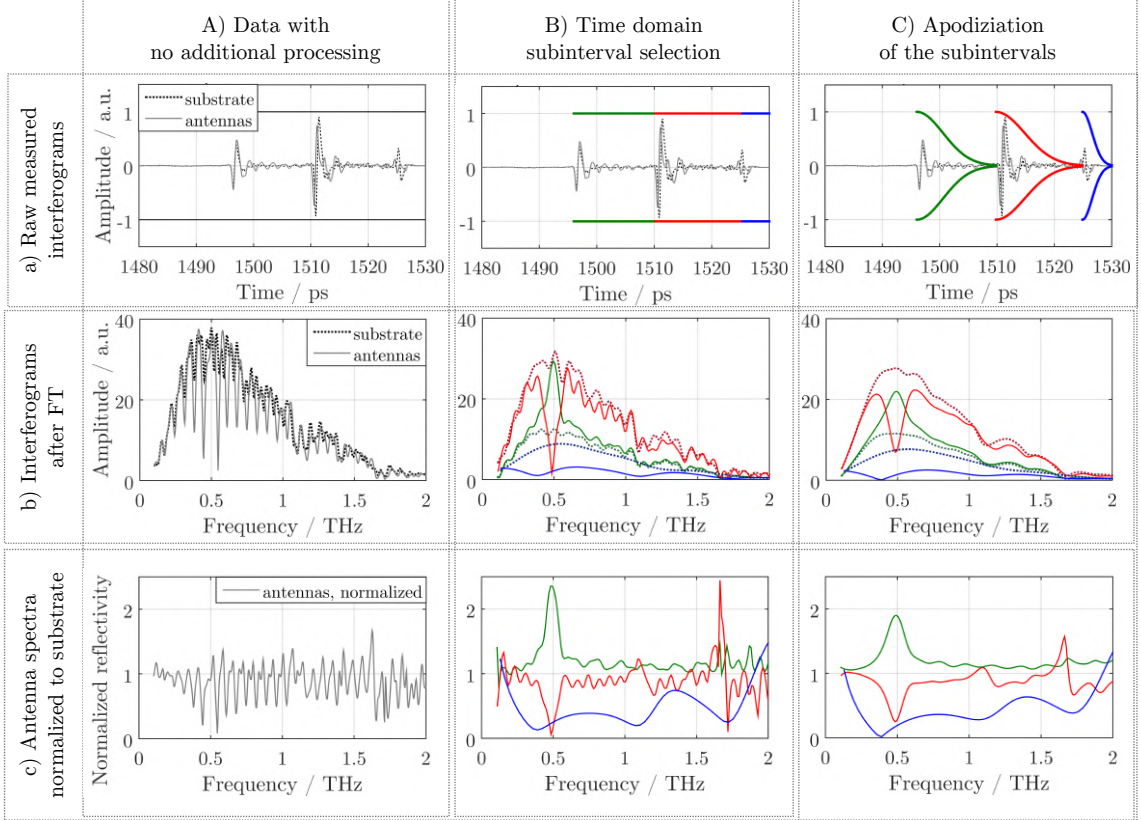
Fig. 9: Taking advantage of the time-domain spectroscopy. A) Non-processed data, the whole measured time domain region has been used for Fourier transform. No antenna resonance can be observed. B) Processed data, only selected parts of the time domain have been considered for each Fourier transform, corresponding to the reflections marked in A. C) Individual time domain regions are multiplied by an apodization function. A reduction of noise elements is visible.

to the reciprocal value of the Gaussian standard deviation. For the processing of the data, a function in this form the has been used:

$$w_n = \exp\left(-\frac{1}{2}\left(\frac{a \cdot n}{N/2}\right)^2\right); n = 0, 1, ...N/2,$$ (17)

where N is the number of time-points which have been recorded within the selected time domain region and $a = 3$. To see the shape of this function and the effects of the apodization curve introduction, see Fig. 9D).

3.4.4 Averaging

As mentioned, in the early starts of this work, solely two points were used for getting information about the measured samples. To improve the reliability of the data processing, the script was adjusted to perform Fourier transform of every measured

point from the conducitivity map. Further, according to the user input, Fourier-transformed interferograms are averaged around several selected points. This provides the user with spectra, which reflect the plasmonic responses of the antenna arrays in a more realistic way. All the results displayed in this thesis are already in their averaged form, which is computed from a (1.1×1.1) mm^2 area, centered around the originally selected points.

4 SAMPLE PREPARATION

In this chapter, the whole fabrication process of the plasmonic antennas will be further explained. There are many ways of fabrication of nanostructures; their usual classification is based on the direction, in which the nanostructures are formed. When the nanostructure is grown on the substrate, the fabrication methods are collectively referred to as *bottom up* techniques. On the other hand, when the nanostructure if formed by the shaping of the deposited material volume, it is denoted as a *top-down* fabrication method.

For the fabrication of the diabolo antennas resonant in the THz region, one of the top-down fabrication methods was chosen, direct laser writing (DLW) (see Fig. 10. This technique has been utilized, as it requires minimal amount of time and causes no problems whned non-conductive substrates are patterned. When compared to other top-down methods such as electron beam lithography or focused ion beam induced techniques, DLW has lower resolution. State of the art DLW tools can fabricate structures with minimal feature dimension of 100 nm in lateral direction or 250 nm in axial direction [45]. However, antennas resonant in the $(0.1 - 1.5)$ THz are far larger, with minimal feature dimension of 4 µm for quartz and 2 µm for silicon substrates. Hence, the resolution of the DLW method is sufficient for the THz diabolo antenna fabrication, as demonstrated in section 4.4.
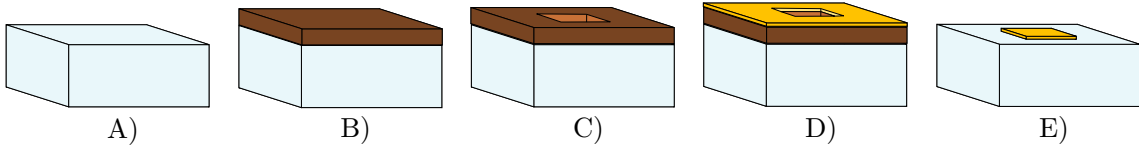

Fig. 10: Lithographic steps of the direct laser writing method: A) Cleaned substrate. B) Substrate with thin layer of the photoresist. C) Photoresist after light exposition and development, topographically modified. D) Metal deposition. E) Prepared nanostructure after the lift-off process.

The main criterion for the selection of the substrates for the sample fabrication has been the non-conductive character of the substrate. Materials with high concentration of free charge carriers could deteriorate the antenna resonances by screening the antenna-induced electric field. Anteriorly, both intrinsic silicon and quartz were used as substrates. Later, quartz substrates were favored due to their lower index of refraction, see section 5.1. The use of quartz substrate also enabled the increase of the antennas while maintaining the same resonance wavelength, as given by equation (12).

All used substrates were thoroughly cleaned in a three-step process; to enhance the cleaning of the substrates, the beakers containing the cleaning fluids were floated

in ultrasonic bath. To provide the cleanest surfaces of the samples, individual steps should last as long as possible. For practical reasons, a five-minute time interval has been chosen for each of the cleaning steps. In the first cleaning step, the samples were dipped in acetone, to remove any excessive organic rests. Afterwards, the cleaning with isopropanole followed, as it removes any redundant acetone. Finally, the sample was cleaned with deionized water in order to get rid of last remainings of isopropanole and dried by nitrogen gas stream.

4.1 Spin-coating

Cleaned substrates were covered with a thin layer of a photoresist by means of spin-coating. First, the sample was heated to remove any moisture from its surface and to allow better distribution of the photoresist. After that, a small volume of the photoresist was dropped on the sample surface – approx. 70 µl/cm^2 of the quartz substrates and around 50 µl/cm^2 on the silicon substrates, in order to cover the whole surface of the substrates. The sample is attached to a holder by a vacuum nozzle, so that it maintains its position while being rotated at high frequencies – several thousands of rounds per minute. With these conditions, the centrifugal force acts on the droplet and the photoresist forms a thin layer with thickness up to 0.5 µm, depending on the used resist and spincoating conditions. After this process, the sample is heated one more time in order to let the photoresist harden.
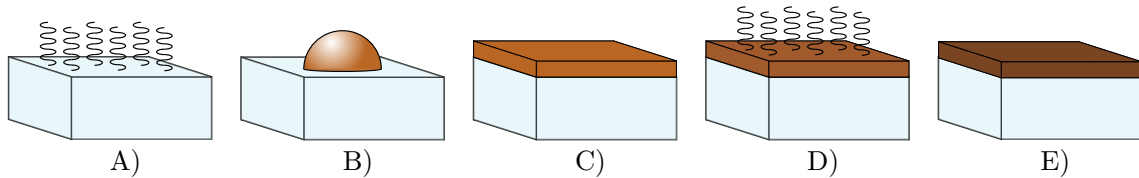

Fig. 11: Spin coating method: A) Substrate pre-bake. B) Droplet of the resist on the substrate, substrate is spinned with high angular frequency. C) Thin resist layer after high-frequential spinning of the substrate. D) Resist after-bake. E) Thin layer of resist ready for exposition.

A photoresist is a light-sensitive material; when exposed to light, it undercomes several structural changes which affect its solubility. Based on this behaviour, two types of photoresists can be distinguished: the positive resists and the negative resists. A *positive* resist is characterized by increased solubility of the light-exposed areas, while the light-exposed parts of a *negative* resist become less soluble than unaffected material. The process of nanostructure fabrication takes advantage of these substances by making them protecting masks for etching of the underlying

substrate or deposition of additonal thin layers of various materials, as described in the next section.

Within this work, a positive photoresist AZ1505 from the MicroChemicals company was used. When spinned with 4000 rpm (revolutions per minute) for 60 s, acceleration of 2000 rpm/s (upcome of revolutions per minute in one second), the photoresist forms a layer with the thickness of ca. 500 nm. Heating of the sample before and after the resist application has been executed with the hotplate set to 100°C, for the time period of 60 s each.

4.2   Sample patterning

There are various different methods of exposing specific intended areas of the photoresist to light. Techniques of optical lithography use non-translucent masks to block the incoming light, therefore effectively providing the selection of exposed areas. This method is useful for fabrication of a large amount of nanostructures, considering that it is very fast and highly replicable. The fabrication of the mask is although necessary, which makes the technique inflexible when series of the same antennas with slight modifications should be prepared, which is the case of this work. Instead, we deployed the technique of direct laser writing.

To pattern the spin-coated photoresist, a DLW instrument from the Heidelberg company has been used, named µPG 101. It uses a laser diod at 375 nm, which enables the patterning of standard photoresists and UV-photoresists as well. The patterning mode with the focal length of 10 mm was used, enabling the writing resolution of appprox. 1 µm.

Ahead of the sample patterning itself, a dose test has been conducted in order to determine what power of the laser is sufficient enough to affect the entire volume of the underlying resist while making sure only designed areas of the photoresist are being exposed to the laser. Nine series of nanoantenna arrays have been exposed with varying parameter of laser energy, see Fig. 12A). Based on this test, the patterning was set to 5 mW and 25% of the laser power. Unwanted ghost-like patterns can be observed at higher percentages of the laser power. Although these were not deep enough to uncover the underlying sample surface, they could affect the lift-off process in a bad manner, making the structure revealing more difficult.

Additionally, a comparison of the two possible patterning modes was done. Anteriorly, a classical exposition mode was used, due to its lower time-consumption. This mode makes every movement of the laserhead worth, as it patterns the sample in both movement directions, as indicated in Fig. 12B) on the left. This results in wave-like structure at the antenna edges. To avoid this effect, a uni-directional
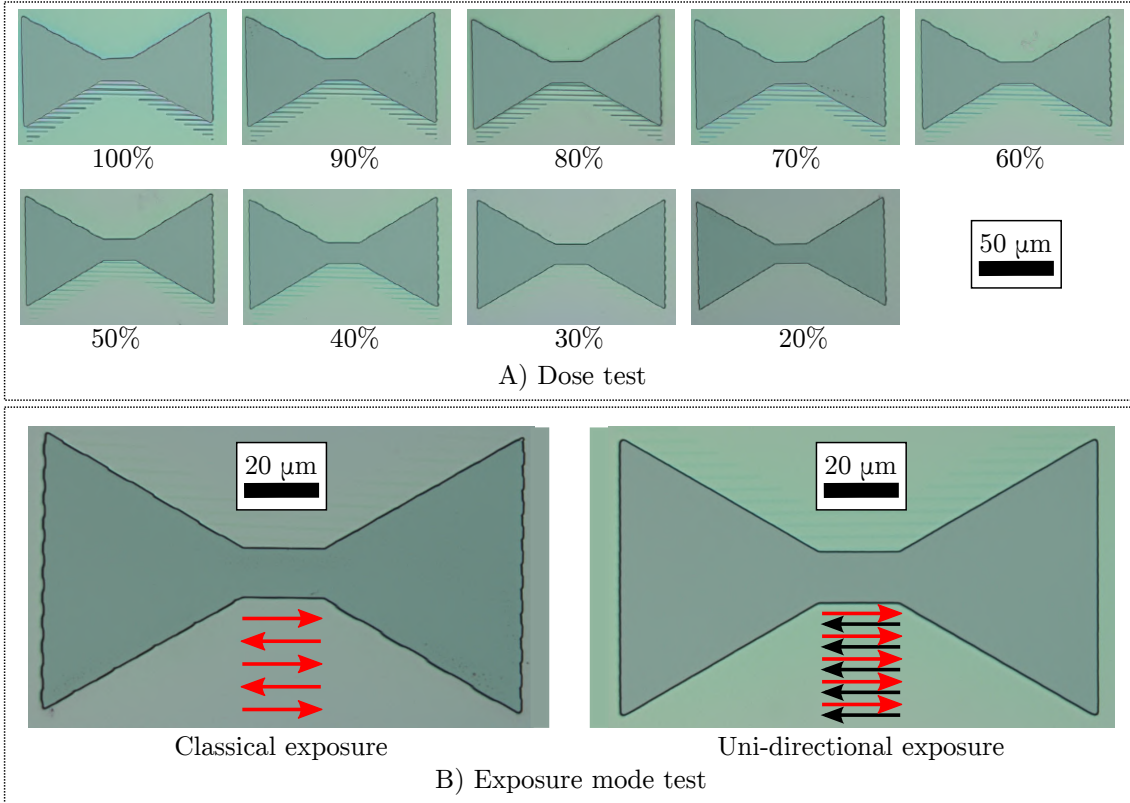
Fig. 12: Testing of the patterning settings. A) Test of various doses for patterning of the photoresist with 5 mW laser. Visible marks have been patterned alongside the structures at high percentage of laser power, therefore the setting of 25% at 5 mW has been used later for the case of this work. B) Comparison of two exposure modes. Red arrows indicate movement connected with patterning while black arrows represent the movements with the laser blanked. The uni-directional mode has been chosen for the fabrication because of its better accuracy – differences are visible especially at the edges of the patterned structures.

patterning mode has been used. Although taking more time – as the laser head returns to the starting line and does not pattern the sample on its way back (black arrows) see the right image of Fig. 12B) – it shows better accuracy for the antenna edges and therefore has been used for further fabrication of antennas.

After the patterning, the sample is put in the developer – a solvent which dissolves some parts of the resist layer, depending on wheter it has or has not been exposed by the light. This process usually takes several tens of seconds and then needs to be stopped. Within this work, a developing reactant AZ 726 MIF has been used, the sample was submerged in it for 30 s and immediately after that, the sample was dipped in the DI water for a minute, to completely terminate the process of resist dissolving. To secure the patterned resist, the sample was additionally baked at 100°C for 60 s. At this point, a mask for metal deposition has been fabricated.

4.3   Metal deposition and lift-off process

In this work, two types of metal deposition have been used, both taking place in the Kurt Lesker evaporator system. First, the sample was covered by ca. 3 nm thick layer of titanium by means of electron beam asissted evaporation. This layer serves as an adhesive for a 140 nm thick layer of gold, deposited by means of thermal evaporation.

The main difference between the two mentioned deposition methods dwells in the melting of the deposited metal. The electron beam evaporation uses high energy electron beam (ca. 10 keV) to locally melt the metal in the crucible. However, in the case of thermal evaporation, the boat, filled with metal, is heated by passing electrical current trough it. The heat of the boat eventually causes the metal in the boat to melt and evaporate. Sample, located directly above the melted metal (regardless of the melting technique) is then very uniformly being covered by the evaporated metal particles. The homogenity of the deposited thin film is dependent on the deposition speed, which commonly reaches values of units of Angströms per second and can be monitored troughout the whole process with an oscillating quartz crystal. Titanium and gold are fairly stable materials regarding the deposition process, hence the deposition rate was set to 0.6 Å/s.
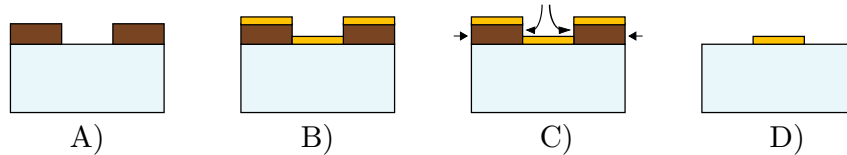

Fig. 13: Lift-off process: A) Sample with patterned resist. B) Metal deposition. C) Lift-off process, in marked spots, the photoresist is dissolved. Therefore, excessive metals are removed from the sample surface. D) Sample after the lift-off process: metallic nanostructure on the substrate.

After the metal deposition, the excessive material shall be removed from the sample substrate in order to unveil the fabricated nanostructures. For this procedure, the lift-off process is used. Sample is put in resist solvent for an amount of time which is sufficient enough to dissolve the photoresist lying under the deposited metal. Within this work, samples were submerged into acetone for ca. $14 - 16$ hours. To support this procedure, additional ultrasound bath of the samples in the solvent is often deployed too, as it helps deattatch the redundant gold film from the structures and hence enhancemes of the edge resolution of the prepared structures. As the angle

of incidende of metallic particles which are being deposited on the sample does not necessarily happen under a right angle, the metal might be deposited on the sides of the resist pattern as well, creating artefacts on the edges of fabricated structures. The ultrasound bath prevents the artefacts from staying at the structure borders.

4.4 Fabricated structures

Gold diabolo antennas were fabricated on quartz and silicon substrates by the means of DLW. Fig. 14 shows several important characteristics of a diabolo antenna, to which we will refer in the following design discussion. Within the antenna designing process, the main parameter was the antenna length L, as it affects the resonance wavelength in a most significant way. The bridge length L_B and bridge width W_B were scaled according to $L/L_B = 1/0.137$ and $L/W_B = 1/0.1$. The wing angle α was kept constant at 60° for all the fabricated antennas. The antenna separations s within the arrays were also dependent on the antenna length L. After fabrication and measurement of the test sample containing different L/s ratios (see section 5.1), the antenna separation of $s = 2.0L$ was maintained for the later fabrication of the samples.

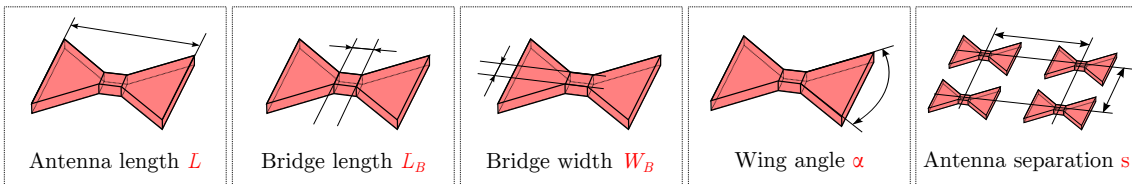| Antenna length L | Bridge length L_B | Bridge width W_B | Wing angle α | Antenna separation s |

Fig. 14: Diabolo antenna parameters preview. For the fabrication of antennas on quartz, the antenna dimensions were scaled according to $L/L_B/W_B = 1/0.137/0.1$. The wing angle $\alpha = 60°$ for all the fabricated antennas. After fabrication and characterization of antenna arrays with different s parameters, the antenna separation s was set to $s = 2.0L$ for futher designs.

To summarize, 9 arrays of antennas with different antenna separation $s = 1.2L$ to $s = 2.8L$ were fabricated on a quartz substrate. To enable an experimental study of the influence of the substrate on the antenna resonances, additional 9 antenna arrays with different antenna separations was fabricated on silicon. As it was proven beneficial to fabricate antennas on quartz substrates (see Fig. 16A)), additional 13 antenna arrays with lengths in the range of $L = 42.1$ µm to $L = 187.1$ µm were fabricated on quartz substrates for further studies.

Fig. 15 shows SEM images of the fabricated diabolo antennas. In panel A), a diabolo antenna of length 98.3 µm is shown, designed for the resonance at 600 GHz. Panels B) and C) depict antennas of lengths 53.7 µm and 42.5 µm, corresponding
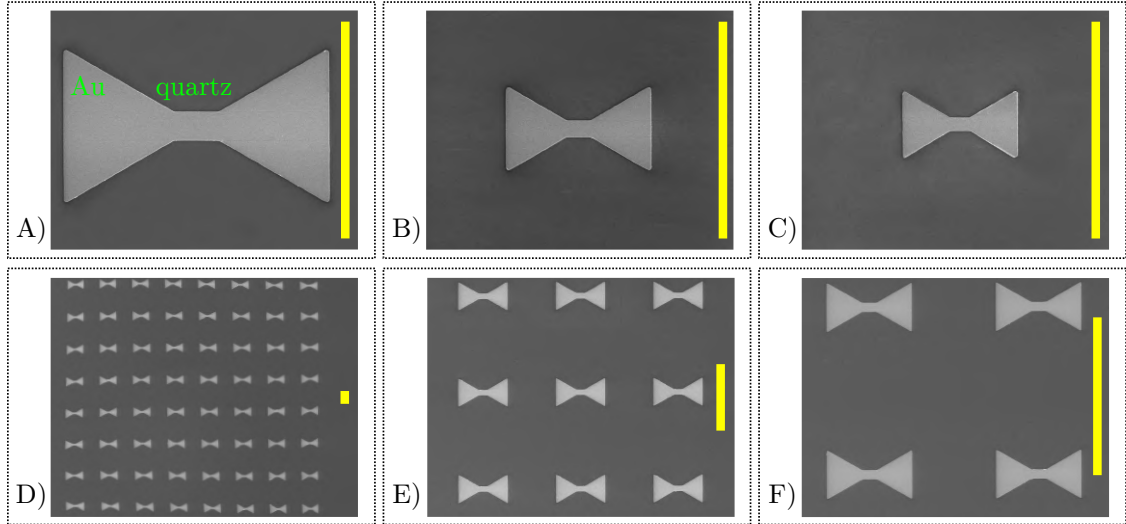
Fig. 15: Scanning electron microscopy images of the fabricated antennas. The yellow vertical scale mark is of length 80 µm in each of the panels. The shown materials are labelled in panel A) with green. A)-C) Individual diabolo antennas with lengths $L = 98.3$ µm, $L = 53.7$ µm and $L = 42.5$ µm, respectively. D) An entire array consisting of 64 antennas (individual antenna is shown in A)) with separation $s = 2.0L$. E)-F) Images of diabolo antenna arrays with antenna separation $s = 2.0L$, corresponding to the individual antennas shown in B) and C).

to resonances at 1100 GHz and 1400 GHz, respectively. Panel D) shows an entire fabricated diabolo antenna array with $s = 2.0L$, containing 64 antennas of lengths 98.3 µm, resonant at 600 GHz. Panels E) and F) include images of the antenna arrays with separation $s = 2.0L$, designed for resonance at 1100 GHz ($L = 53.7$ µm as in B)) and 1400 GHz ($L = 42.5$ µm as in C)), respectively.

The accuracy of the DLW antenna fabrication method has been evaluated by a comparison of the designed and actual measured values of several antenna parameters included in Fig. 14. For the measurement of the antenna dimensions, optical microscope images were analyzed using a graphical analysis tool Gwyddion to get the average of L, L_B and W_B dimensions of the fabricated antennas. These are marked as "actual" and compared to their diesign values in the Table 4.1. To summarize, every antenna length L, with two exceptions, differs from the designed dimension in less than 0.5 µm, which is a good result, considering the patterning system resolution of approx. 1 µm. The bridge lengths L_B deviate from the designed values a little more, as the edge between the antenna wing and the bridge could not be fabricated as sharp as designed. The same agreement has been found between the design and actual values of the bridge width W_B dimensions. Based on the results of this comparison, the DLW method can be described as a reliable way of producing micrometer-scale antennas with resonances in the frequency region (0.2-1.4) THz.

resonance / GHz		L / µm		bL / µm		bW / µm	
designed	actual	designed	actual	designed	actual	designed	actual
315	308	187.14	188.30	32.42	32.40	18.71	18.00
350	342	168.43	169.80	29.18	29.00	16.84	16.70
425	425	138.71	139.50	24.03	23.60	13.87	13.20
500	496	117.90	118.70	20.42	20.30	11.79	11.60
600	602	98.25	98.30	17.02	16.20	9.83	10.60
700	696	84.21	84.80	14.59	14.10	8.42	9.20
800	802	73.69	74.00	12.76	12.40	7.37	8.10
900	897	65.50	65.90	11.35	10.50	6.55	6.50
1000	1003	58.95	59.10	10.21	9.50	5.90	6.10
1100	1109	53.59	53.70	9.28	8.90	5.36	5.80
1200	1180	49.13	49.30	8.51	8.13	4.91	5.24
1300	1322	45.35	45.60	7.85	7.13	4.53	4.93
1400	1404	42.11	42.50	7.29	6.48	4.21	4.40

Tab. 4.1: Summary of the designed and measured antenna dimensions and resonances corresponding to them. The wing angle was kept constant at the value $\alpha = 60°$, antenna separation $s = 2L$. Resonance peak maxima were collected directly from the measured spectra, in the last two cases not identified (NI) due to unreliability of the measured datasets, see also Fig. 17.

5 THz-TDS RESULTS

As discussed in the introductory plasmonic chapters, the resonant wavelength of a plasmonic antenna may be altered by the antenna size, shape, its dielectric surroundings,... . In this chapter, the influence of the mentioned factors on the resonance wavelengh of the antenna array will be experimentally demonstrated and analyzed. In the first part of the experimental work, antenna arrays with various inter-antennal separations have been fabricated on quartz and silicon substrates. In the second part, the influence of the antenna size on the resonant wavelength of an diabolo antenna has been studied.

5.1 The influence of the antenna separation on different substrates

For an experimental study of the influence of the substrate on the resonance wavelength of a diabolo antenna, THz-TDS spectroscopic measurements of various antenna arrays with different antenna separation on both silicon ($n_{\mathrm{Silicon}} = 3.4$) and quartz substrates ($n_{\mathrm{Quartz}} = 1.9$) were performed. Nine antenna separation variations have been probed, ranging from $s = 1.2L$ to $s = 2.8L$ on both substrate types. The size of the antennas was kept constant for all arrays on silicon and quartz, with $L_{\mathrm{Silicon}} = 128$ µm and $L_{\mathrm{Quartz}} = 67.5$ µm. The results of these measurements are depicted in Fig. 16.

The Fig. 16A) shows the spectra of the antenna arrays on silicon (left) and quartz (right) substrates. The results clearly show the dominance of yielded resonances from antennas on quartz substrate. Two explanations of this result can be provided. First, a metallic antenna, supporting a LSP resonance, creates an electric field around it, as discussed in chapter 2. In a substrate with high refractive index (hence higher density of free electrons), such as silicon, the conduction electrons are forced by the mentioned electric field to reorganize and eventually partially screen the LSP ocurring at the air-antenna interface. Hence, the observed magnitude of the normalized reflectivity is smaller with silicon than compared to quartz, material with lower refractive index. The second explanation is more straight forward: the lower refractive index of quartz enables the use of bigger structures for the resonance at the same wavelength, according to the equation (12). Bigger antennas have bigger scattering cross-sections, and therefore, more signal is detected from the antennas, resulting into larger magnitude of normalized reflectivity values.

The design of the antenna arrays is shown in Fig. 16B), where s denotes the distance between neighboring antenna centers and L the antenna length, as estab-
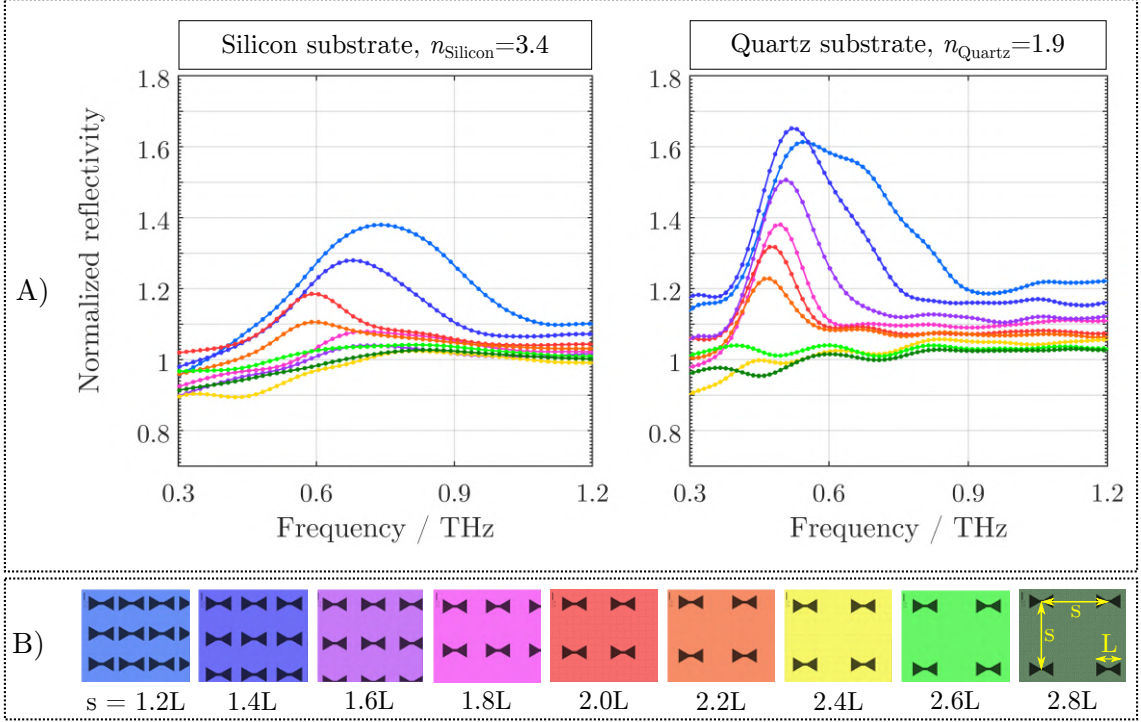
Fig. 16: THz-TDS of the diabolo antenna arrays. A) Spectra of arrays on silicon and quartz substrate for different antenna separations s. The color of the spectra corresponds to the array of the same color illustrated in panel B. B) Design of the antenna arrays. Antenna lengths $L_{\text{Silicon}} = 128$ µm and Quartz $= 67.5$ µm were kept constant within all the substrate-corresponsive arrays. The general design of the antenna dimensions is specified in the section 4.4.

lished in Fig. 14. The colors of the insets correspond to the colors of the spectra shown in panel A). On both substrates we find that the resonance peaks intensify with decreasing antenna separation s, while the resonance slightly shifts to higher frequencies. For $s < 2.0L$ we additionally see a broadening of the resonance. On the other hand, for $s > 2.0L$ we find that the signal becomes too weak to be detected. The increasing peak height with decreasing separation s can be explained simply by the fact that more antennas are located in the THz beam. For comparison, with the beam spot of 2.1 mm and quartz substrate, 137 full antennas fit in the beam spot with $s = 1.2L$, but only 20 full antennas fit for the setting $s = 2.8L$. The blueshift and broadening of the antenna resonance can be explained by transverse electromagnetic coupling of the antennas, which has been previously observed and explained, for example, with infrared antenna arrays [46]. The antenna arrays with separation $s = 2.0L$ on quartz seemed to be most appropriate, as they provide large signals without being disturbed too much by transverse near-field coupling. Hence, this array-type has been used for further experiments.

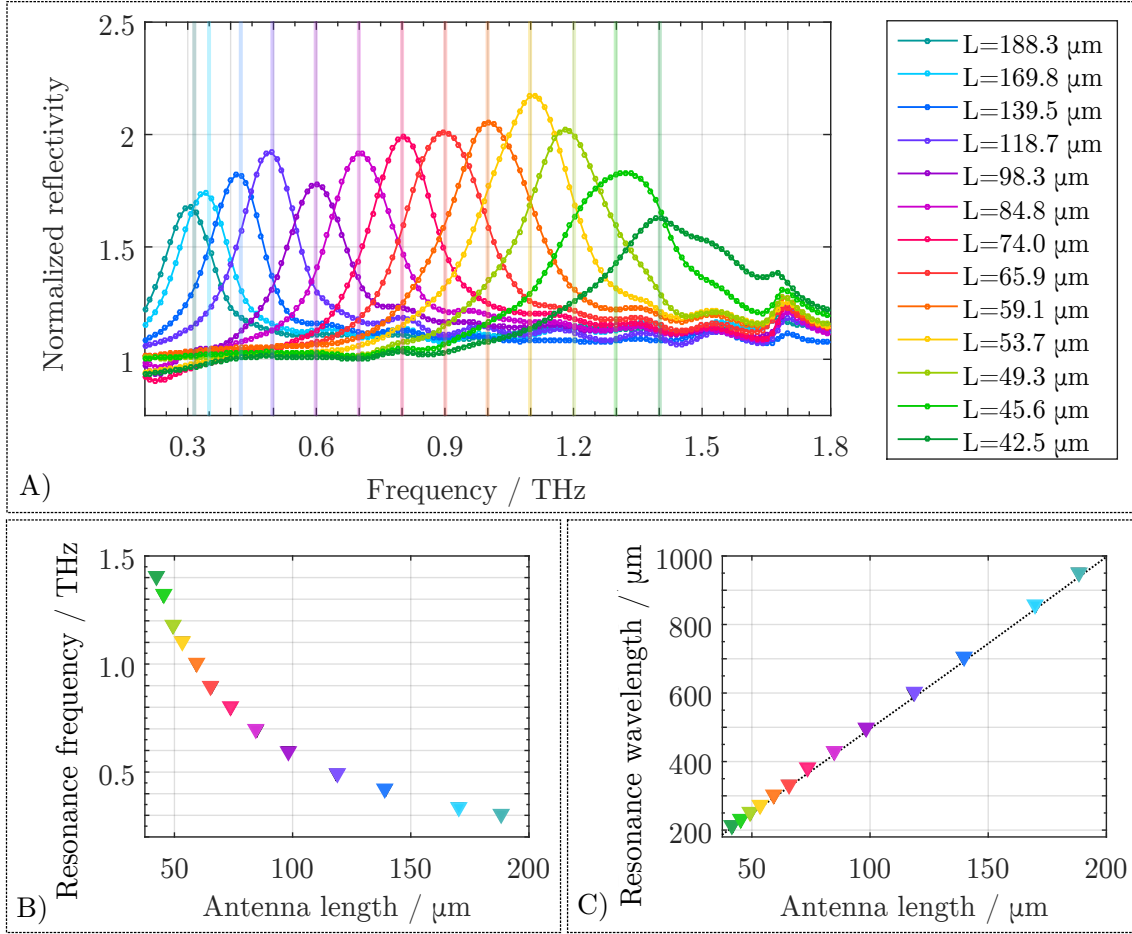## 5.2 Influence of the antenna size

Fig. 17: Antenna resonance tuning by the antenna size variation. A) THz-TDS spectra of antenna arrays ($s = 2.0L$) on quartz substrate. Vertical lines indicate the resonance frequency according to the antenna design. B) Resonance frequency versus antenna length, the maxima from spectra shown in A) are used. C) Resonant wavelength versus antenna length. The dotted line is fitted to the measured points (triangles), $\lambda_{res} = 5.06L$. Colors of the triangles correspond to the color of the spectra shown in panel A).

To experimentally examine the impact of the antenna size on the resonance wavelength of a diabolo antenna, 13 arrays of antennas were fabricated on quartz substrates by the means of DWL (see chapter 4) and mesured by the THz-TDS system.

Fig. 17 shows time domain spectroscopy results obtained for antenna arrays where the size of the antennas was varied, while the distance between the antennas was set to $s = 2.0L$. The shape of the antennas was the same in all arrays, as described in the section 4.4. The variations of the antenna size are denoted by the antenna length in this figure, as the antenna length is the main parameter of a

diabolo antenna; antenna length contributes to the resonance wavelength position in most significant way, as the direction of this parameter was parallel with the polarization of the THz beam used for TDS. Fig. 17A) shows THz-TDS spectra of the antenna arrays. As the antenna length increases, a shift of the antenna resonance to higher frequencies can be observed. With respect to equation (12), a relationship between the resonance frequency f_{res} and antenna length can be derived:

$$f_{\mathrm{res}} \cong \frac{1}{2Ln_{\mathrm{eff}}}, \tag{18}$$

which supports the reciprocal proportion of the two quantities. Fig. 17B) shows the spectral peak positions as a function of the antenna length and the tendency resembles of a inverse proportionality. Indeed, Fig. 17C) demonstrates the linear relationship between the antenna length and the resonance wavelength ($\lambda_{\mathrm{res}} \cong 1/f_{\mathrm{res}}$). The measured resonances (marked as triangles) have been fitted and a linear function was obtained:

$$\lambda_{\mathrm{res}} = 5.06L, \tag{19}$$

marked with the dotted line. For dipole antennas, a linear dependence is expected, see equation (12). Hence, the observed factor of 5.06 between the resonance wavelength and the antenna length originates in the materials, which form the arrayed antennas and the substrate (gold and quartz, respectively).

By revealing the linear relation (19), the fabrication of diabolo antennas with predefined resonance wavelength will be easier as the designs can be inspired by the results achieved within this work.

6 CONCLUSIONS

The aim of this work was to support the running PETER project, which deals with the Plasmon Enhanced Terahertz Electron Paramagnetic Resonance, by the fabrication and characterization of diabolo antennas.

The first two chapters are introductory, giving the basic information about the history and theoretical background of the field of plasmonics. The resonances of the localised plasmon polariton have been introduced, as this is the fundamental aspect of the theory on which this work is based.

The third chapter is focused on the description of the tool used for THz time-domain spectroscopy. As this tool has been designed for different purposes, it has never been used for the THz TDS before. Hence, a detailed technical description of its individual features and settings is provided to facilitate the work with the tool. Then, an introduction to the processing of the data measured by this tool is provided. Based on the work of Dr. Curdin Maissen, a computer script has been developed by the author, which enables the analysis of the yielded data in order to observe plasmonic responses of the antennas resonant in the THz frequency region in high quality, free of unwanted noise and resonances.

Chapter 4 describes in detail the fabrication process of the diabolo antennas by the means of direct laser writing. The basic principles of individual fabrication steps are explained and followed by a summary of produced samples. Eventually, an evaluation of the accuracy of the direct laser writing method is provided, proving that for the fabrication of micrometer-scale antennas, the chosen technique is reliable.

The last chapter deals with the results of the THz-TDS measurements. These were provided by the tool described in chapter 3, and processed by the developed script. First, the influence of the substrate is demonstrated by a comparison of plasmonic resonances yielded from antennas on silicon and quartz substrates. It has been shown that the resonance is more significant in the measurement of the antennas placed on a quartz substrate. This is explainable by the antenna size and also by lower refraction index of the substrate material, which leads to smaller screening of the plasmonic responses from the antennas. Within the same experiment, the dependence of the resonant wavelength on the antenna separation is demonstrated. An ideal separation between the diabolo antennas has been established, providing sufficiently large signals while lacking the disturbances caused by the coupling of the neighboring antennas, which result into broad resonance peaks. Eventually, a study of the antenna size impact on the resonance wavelength has been performed. Based on this experiment, a relationship between the antenna length and the resonance wavelength has been introduced, which will facilitate the fabrication of diabolo antennas with precise resonance wavelength.

BIBLIOGRAPHY

[1] PETER project website. Available at www.peter-instruments.eu.

[2] Novotny, L. and Hecht, B. *Principles of Nano-Optics.* Cambridge University Press, **2006**. ISBN 9780511813535. doi:10.1017/CBO9780511813535.

[3] Maier, S. *Plasmonics - Fundamentals and Applications.* Springer, **2007**. ISBN 9781441941138. doi:10.1007/0-387-37825-1.

[4] Raether, H. *Surface plasmons on smooth and rough surfaces and on gratings.* No. 111 in Springer tracts in modern physics. Springer, **1988**. ISBN 9783540173632. doi:10.1007/BFb0048317.

[5] Wood, R. XLII. On a remarkable case of uneven distribution of light in a diffraction grating spectrum. *The London, Edinburgh, and Dublin Philosophical Magazine and Journal of Science*, 4 (21), **1902**, pp. 396–402. doi:10.1080/14786440209462857.

[6] Ritchie, R. H., Arakawa, E. T., Cowan, J. J., and Hamm, R. N. Surface-Plasmon Resonance Effect in Grating Diffraction. *Physical Review Letters*, 21, **1968**, pp. 1530–1533. doi:10.1103/PhysRevLett.21.1530.

[7] Zayats, A. V., Smolyaninov, I. I., and Maradudin, A. A. Nano-optics of surface plasmon polaritons. *Physics Reports*, 408 (3), **2005**, pp. 131 – 314. doi:10.1016/j.physrep.2004.11.001.

[8] Mie, G. Beiträge zur Optik trüber Medien, speziell kolloidaler Metallösungen. *Annalen der Physik*, 330 (3), **1908**, pp. 377–445. doi:10.1002/andp.19083300302.

[9] Tang, L., Ekin Kocabas, S., Latif, S., *et al.* Nanometre-scale germanium photodetector enhanced by a near-infrared dipole antenna. *Nature Photonics*, 2, **2008**, pp. 226–229. doi:10.1038/nphoton.2008.30.

[10] Challener, W., Peng, C., V. Itagi, A., *et al.* Heat-assisted magnetic recording by a near-field transducer with efficient optical energy transfer. *Nature Photonics*, 3, **2009**, pp. 220–224. doi:10.1038/nphoton.2009.26.

[11] Atwater, H. and Polman, A. Plasmonics for Improved Photovoltaic Devices. *Nature materials*, 9, **2010**, p. 865. doi:10.1038/nmat2866.

[12] Kamakura, R., Takeishi, T., Murai, S., *et al.* Surface-Enhanced Infrared Absorption for the Periodic Array of Indium Tin Oxide and Gold Microdiscs: Effect of in-Plane Light Diffraction. *ACS Photonics*, 5 (7), **2018**, pp. 2602–2608. doi:10.1021/acsphotonics.7b01265.

[13] Weber, K., Nesterov, M. L., Weiss, T., *et al.* Wavelength Scaling in Antenna-Enhanced Infrared Spectroscopy: Toward the Far-IR and THz Region. *ACS Photonics*, 4 (1), **2017**, pp. 45–51. doi:10.1021/acsphotonics.6b00534.

[14] Wang, P., Xia, M., Liang, O., *et al.* Label-Free SERS Selective Detection of Dopamine and Serotonin Using Graphene-Au Nanopyramid Heterostructure. *Analytical Chemistry*, 87 (20), **2015**, pp. 10255–10261. doi:10.1021/acs.analchem.5b01560.

[15] D'Andrea, C., Bochterle, J., Toma, A., *et al.* Optical Nanoantennas for Multiband Surface-Enhanced Infrared and Raman Spectroscopy. *ACS Nano*, 7 (4), **2013**, pp. 3522–3531. doi:10.1021/nn4004764.

[16] Crozier, K. B., Sundaramurthy, A., Kino, G. S., and Quate, C. F. Optical antennas: Resonators for local field enhancement. *Journal of Applied Physics*, 94 (7), **2003**, pp. 4632–4642. doi:10.1063/1.1602956.

[17] L. Barnes, W., Dereux, A., and W. Ebbesen, T. Surface Plasmon Subwavelength Optics. *Nature*, 424, **2003**, pp. 824–830. doi:10.1038/nature01937.

[18] Schnell, M., Garcia-Etxarri, A., Huber, A., *et al.* Controlling the near-field oscillations of loaded plasmonic nanoantennas. *Nature Photonics*, 3, **2009**, pp. 287–291. doi:10.1038/nphoton.2009.46.

[19] Kuttner, C., Mayer, M., Dulle, M., *et al.* Seeded Growth Synthesis of Gold Nanotriangles: Size Control, SAXS Analysis, and SERS Performance. *ACS Applied Materials & Interfaces*, 10 (13), **2018**, pp. 11152–11163. doi:10.1021/acsami.7b19081.

[20] Rang, M., Jones, A. C., Zhou, F., *et al.* Optical Near-Field Mapping of Plasmonic Nanoprisms. *Nano Letters*, 8 (10), **2008**, pp. 3357–3363. doi:10.1021/nl801808b.

[21] Mazzotta, F., Johnson, T. W., Dahlin, A. B., *et al.* Influence of the Evanescent Field Decay Length on the Sensitivity of Plasmonic Nanodisks and Nanoholes. *ACS Photonics*, 2 (2), **2015**, pp. 256–262. doi:10.1021/ph500360d.

[22] De Angelis, F., Malerba, M., Patrini, M., *et al.* 3D Hollow Nanostructures as Building Blocks for Multifunctional Plasmonics. *Nano Letters*, 13 (8), **2013**, pp. 3553–3558. doi:10.1021/nl401100x.

[23] Diao, Z., Kraus, M., Brunner, R., *et al.* Nanostructured Stealth Surfaces for Visible and Near-Infrared Light. *Nano Letters*, 16 (10), **2016**, pp. 6610–6616. doi:10.1021/acs.nanolett.6b03308.

[24] Abid, M. I., Wang, L., Chen, Q.-D., *et al.* Angle-multiplexed optical printing of biomimetic hierarchical 3D textures. *Laser & Photonics Reviews*, 11 (2), **2017**, p. 1600187. doi:10.1002/lpor.201600187.

[25] Kumar, P., Nagpal, K., and Gupta, B. K. Unclonable Security Codes Designed from Multicolor Luminescent Lanthanide-Doped Y2O3 Nanorods for Anticounterfeiting. *ACS Applied Materials & Interfaces*, 9 (16), **2017**, pp. 14301–14308. doi:10.1021/acsami.7b03353.

[26] Baldassarre, L., Sakat, E., Frigerio, J., *et al.* Midinfrared Plasmon-Enhanced Spectroscopy with Germanium Antennas on Silicon Substrates. *Nano Letters*, 15 (11), **2015**, pp. 7225–7231. doi:10.1021/acs.nanolett.5b03247.

[27] Yoo, D., Mohr, D. A., Vidal-Codina, F., *et al.* High-Contrast Infrared Absorption Spectroscopy via Mass-Produced Coaxial Zero-Mode Resonators with Sub-10 nm Gaps. *Nano Letters*, 18 (3), **2018**, pp. 1930–1936. doi:10.1021/acs.nanolett.7b0529.

[28] Qi, Z., Zhai, Y., Wen, L., *et al.* Au nanoparticle-decorated silicon pyramids for plasmon-enhanced hot electron near-infrared photodetection. *Nanotechnology*, 28 (27), **2017**, p. 275202. doi:10.1088/1361-6528/aa74a3.

[29] Sieger, M. and Mizaikoff, B. Toward On-Chip Mid-Infrared Sensors. *Analytical Chemistry*, 88 (11), **2016**, pp. 5562–5573. doi:10.1021/acs.analchem.5b04143.

[30] Li, D., Li, D.-W., Fossey, J. S., and Long, Y.-T. Portable Surface-Enhanced Raman Scattering Sensor for Rapid Detection of Aniline and Phenol Derivatives by On-Site Electrostatic Preconcentration. *Analytical Chemistry*, 82 (22), **2010**, pp. 9299–9305. doi:10.1021/ac101812x.

[31] Zhu, L., Wang, Y., Liu, Y., and Yue, C. Design and Analysis of Ultra Broadband Nano-absorber for Solar Energy Harvesting. *Plasmonics*, 13, **2017**. doi:10.1007/s11468-017-0533-1.

[32] Liu, X., M. Osgood Jr, R., Vlasov, Y., and M J Green, W. Mid-infrared optical parametric amplifier using silicon nanophotonic waveguides. *Nature Photonics*, 4, **2010**. doi:10.1038/nphoton.2010.119.

[33] Cui, D., Xu, J., Zhu, T., *et al.* Harvest of near infrared light in PbSe nanocrystal-polymer hybrid photovoltaic cells. *Applied Physics Letters*, 88 (18), **2006**, p. 183111. doi:10.1063/1.2201047.

[34] Lee, D.-K., Kang, J.-H., Lee, J.-S., *et al.* Highly sensitive and selective sugar detection by terahertz nano-antennas. *Scientific reports*, 5, **2015**. doi:10.1038/srep15459.

[35] Yamaguchi, S., Fukushi, Y., Kubota, O., *et al.* Brain tumor imaging of rat fresh tissue using terahertz spectroscopy. *Scientific Reports*, 6, **2016**, p. 30124. doi:10.1038/srep30124.

[36] Piccoli, R., Rovere, A., Toma, A., *et al.* Plasmon Coupling of Gold Nanorods at Short Distances and in Different Geometries. Chapter in *Terahertz Spectroscopy – A Cutting Edge Technology*, , **2017**. doi:10.5772/66349.

[37] Toma, A., Tuccio, S., Prato, M., *et al.* Squeezing Terahertz Light into Nanovolumes: Nanoantenna Enhanced Terahertz Spectroscopy (NETS) of Semiconductor Quantum Dots. *Nano Letters*, 15 (1), **2015**, pp. 386–391. doi:10.1021/nl503705w.

[38] Ueno, K., Nozawa, S., and Misawa, H. Surface-enhanced terahertz spectroscopy using gold rod structures resonant with terahertz waves. *Opt. Express*, 23 (22), **2015**, pp. 28584–28592. doi:10.1364/OE.23.028584.

[39] Ligmajer, F., Hrtoň, M., Šikola, T., and Hillenbrand, R. *Plasmonic structure design for PE EPR microscopy.* Deliverable D1.2, H2020 FET OPEN project PETER (GA#767227), **2018**. Avaliable at https://www.peter-instruments.eu/file/d1-2-ps-design-for-plasmon-enhanced-epr-20181229-pdf/.

[40] Park, H.-R., Ahn, K. J., Han, S., *et al.* Colossal Absorption of Molecules Inside Single Terahertz Nanoantennas. *Nano Letters*, 13 (4), **2013**, pp. 1782–1786. doi:10.1021/nl400374z.

[41] Davies, A. G., Burnett, A. D., Fan, W., *et al.* Terahertz spectroscopy of explosives and drugs. *Materials Today*, 11 (3), **2008**, pp. 18 – 26. doi:https://doi.org/10.1016/S1369-7021(08)70016-6.

[42] Zhang, H., Siegrist, K., Plusquellic, D. F., and Gregurick, S. K. Terahertz Spectra and Normal Mode Analysis of the Crystalline VA Class Dipeptide Nanotubes. *Journal of the American Chemical Society*, 130 (52), **2008**, pp. 17846–17857. doi:10.1021/ja805581n.

[43] Chatterjee, S., Grunwald, T., Köhler, D., *et al.* THz measurements of the optical response in a two-dimensional electron gas. *physica status solidi c*, 6 (2), **2009**, pp. 453–456. doi:10.1002/pssc.200880337.

[44] Huth, F. *Nano-FTIR - Nanoscale Infrared Near-Field Spectroscopy.* PhD Thesis, University of the Basque Country (Supervisor: Dr. Rainer Hillenbrand), **2015**.

[45] Fischer, J. *Three-dimensional optical lithography beyond the diffraction limit.* PhD Thesis, Karlsruhe Institute of Technology (Supervisor: Prof. Martin Wegener), **2012**.

[46] Weber, D., Albella, P., Alonso-González, P., *et al.* Longitudinal and transverse coupling of gold nanoantenna arrays: long range versus short range interaction regimes. *Opt. Express*, 19 (16), **2011**, pp. 15048–15061. doi:10.1021/nl900034v.

APPENDIX A

CERTIFICATE OF CALIBRATION

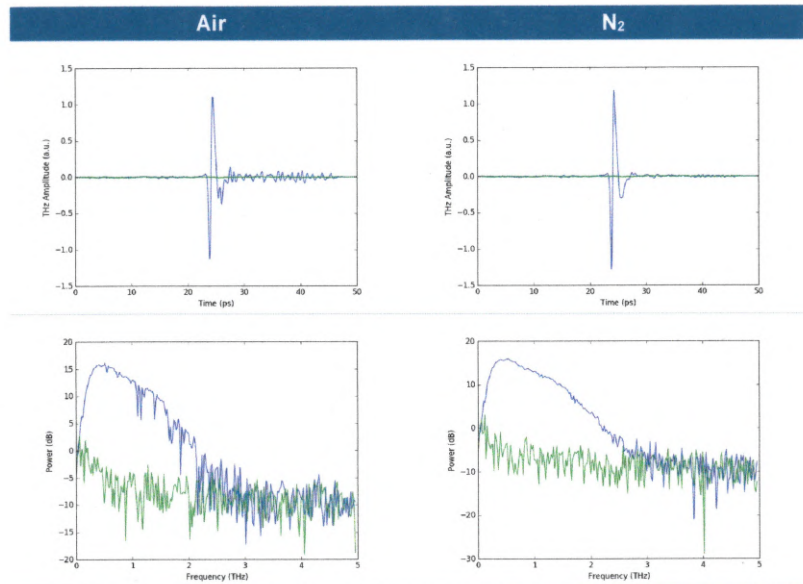**Certificate Number:** ONX0001_311016
Product: ONYX – Graphene & 2D Materials Quality Inspector
Serial Number: ONX0001
Date of calibration: 31th October, 2016

CALIBRATION DATA

	Air	N_2		Air	N_2
MAXIMUM (a.u.)	1.113	1.113	**POSITION** (ps)	24.475	24.475
MINIMUM (a.u.)	-1.127	-1.127	**POSITION** (ps)	23.925	23.925
BW (THz)	2.8	3.1	**SPOT SIZE** (mm)	2.1	
SNR (dB)	58.9	63.6	**NOISE RMS** (dB)	-48	-48

Air	N_2

Noain, 31th October 2016

Done by
D. David Etayo

Approved by
D. Albert Redo-Sanchez
Terahertz
Technology Manager

das·nano

A